Article

Europium Doping Effects on the Properties of CsPbBr$_3$ Nanocrystals: *In-situ* vs. *Ex-situ* Synthetic Path Analysis

Hila Shalom[1], Raanan Carmieli[2], Pini Shekhter[3], Lena Yadgarov[1,]*

1. Department of Chemical Engineering, Ariel University, Ariel, 4076414, Israel;
2. Department of Chemical Research Support, Weizmann Institute of Science, Rehovot 7610001, Israel;
3. Center for Nanoscience and Nanotechnology, Tel-Aviv University, Ramat Aviv, Tel Aviv 6997801, Israel;
    Email: lenay@ariel.ac.il.

Abstract:

Metal halide perovskites (MHPs), particularly CsPbBr$_3$ nanocrystals (NCs), attract significant interest due to their remarkable optoelectronic properties. These properties make them ideally suited for applications such as photovoltaics and ionizing radiation detectors. However, CsPbBr$_3$ NCs suffer from poor luminescence efficiency and short service life. Doping with rare earth (RE) elements, especially europium (Eu), has emerged as a viable method for solving these problems because of their unique electronic structure. Doping with RE improves luminescence efficiency and extends the service life of the MHPs, enhancing their optoelectronic properties and catalytic capabilities. This study examines the effects of *in-situ* and *ex-situ* europium doping on the structural, optical, and photocatalytic properties of CsPbBr$_3$ NCs. *In-situ* doping was achieved by introducing the dopant during the NC synthesis, while *ex-situ* doping involved adding the dopant to pre-prepared NCs via sonochemical synthesis with an ultrasonic bath. The doped NCs exhibit enhanced emission and boosted photocatalytic activity, showcasing the multifaceted benefits of Eu ions doping. The study concludes that *in-situ* europium doping, particularly at 5 wt%, significantly enhances the structural and functional characteristics of CsPbBr$_3$ NCs, offering a promising approach for improving their performance in optoelectronic and photocatalytic applications.

1. Introduction

Metal halide perovskites (MHPs) have rapidly attracted significant scientific attention due to their photo-physical and optoelectronic properties.[1–3] They have high photoluminescence quantum yields (PLQYs), a narrow emission width, a widely tunable bandgap and emission wavelength in the visible range, high charge-carrier mobility, and a long diffusion length.[4–8] MHPs also have the advantage of being simple to manufacture, which has led to their use in numerous fields, including photovoltaics[9,10], photodetectors[11,12], light-emitting diodes[13,14], lasers[15,16], solar-to-fuel energy conversion systems[17] and ionizing radiation detectors.[18]

Among the family of MHP NCs, CsPbBr$_3$ NCs are well-known for their distinctive features. These include low-temperature processability, relative stability at room temperature in air, and a highly emissive crystalline phase. The CsPbBr$_3$ perovskite has outstanding luminescence properties, including an

extremely high quantum yield of ~ 90% without any optimization and a narrow emission bandwidth (12–42 nm) in the visible light region.[19] However, CsPbBr$_3$ NCs have poor luminescence efficiency[20] and short service life.[21] Doping strategies of CsPbBr$_3$ NCs are considered an effective means for alleviating these drawbacks and can also help reduce the toxicity of these nanocrystals.[22–27]

Rare earth (RE) elements have gained attention among various dopants due to their unique optical, electrical, and catalytic properties. The incorporation of RE elements into nanomaterials can enhance their suitability for a wide array of advanced technological applications.[28] These elements are characterized by their unique energy transitions and optical properties, which arise from their specific 4f electronic structure.[29] One of the RE elements that increase luminescence emission is europium (Eu).[30] Europium can exist in two oxidation states (Eu^{2+} or Eu^{3+}) depending on the host material. The doping of MHPs with Eu^{2+} has broad emission from the parity-allowed transition 4f^{6}5d^1 → 4f^7, which produces a wide emission range in the blue-green-yellow or red band.[31] Contrasty, the MHPs doping of Eu^{3+} has sharp emission lines that originate from the 4f^6 → 4f^6 transition in the red region.[31–33] Therefore, europium doping allows for modification of the PL emission of the CsPbBr$_3$ NCs due to an internal energy transition in the Eu ion.[34] The ionic radius of Eu ions (117 pm for Eu^{2+} and 94.7 pm for Eu^{3+}) is relatively small compared to Pb^{2+} (119 pm).[35] Hence, upon doping, the lattice of CsPbBr$_3$ NCs shrinks due to the Eu ion partially replacing the Pb^{2+} ion. Consequently, a lesser strain in the NCs' lattice increased the stability of europium-doped CsPbBr$_3$ NCs.[32,36]

Here, we compare the effects of *in-situ* and *ex-situ* europium doping on the properties of CsPbBr$_3$ NCs. The CsPbBr$_3$ NCs are synthesized using a hot injection method conducted at high temperatures. *In-situ* doping involves incorporating dopants directly into the nanocrystals during their synthesis.[37] As a result, *in-situ* doping ensures a more uniform and effective distribution of dopant ions within the CsPbBr$_3$ lattice.[38] This uniform distribution helps minimize local strain and reduces the likelihood of creating large defects, thereby enhancing the overall structural stability of the nanocrystals.[37–39] In *ex-situ* doping, like the post-synthetic cation exchange method, the dopant atoms are introduced to the nanocrystals after their initial synthesis,[40].[41] The halide perovskite NCs system is known for topotactic cation exchange.[42–44] Since the dopants are introduced into pre-synthesized nanocrystals, their incorporation is more time-consuming and can be less uniform, potentially leading to localized strain and surface defect formation.[39,41] However, the stability of *ex-situ* doped nanocrystals can also be affected by the processing conditions, including the choice of solvent and doping elements used.[41]

In this study, we contrast the impact of *in-situ* and *ex-situ* Eu ions doping on CsPbBr$_3$ NCs to assess the effects on their structural, optical, and electronic properties. *In-situ* doping was achieved by introducing the dopant during NC synthesis through the hot injection method. In contrast, *ex-situ* doping involved adding the dopant to pre-prepared NCs using sonochemical synthesis with an ultrasonic bath. Comprehensive characterization, including transmission electron microscopy (TEM), X-ray powder diffraction (XRD), X-ray photoelectron spectroscopy (XPS), UV-Vis spectrophotometry, and fluorescence measurements, provided detailed insights into the composition, crystallinity, surface chemistry, optical behavior, and functional capabilities of the synthesized NCs. Additionally, the photocatalytic performance of Eu-doped CsPbBr$_3$ NCs was assessed by their ability to degrade methyl orange in an ethanol-toluene solution under solar simulation. Our findings demonstrate that different doping methods by Eu ions lead to varied effects on the characteristics and performance of the NCs. This work paves the way for advancing

our understanding of how to stabilize and enhance the optoelectronic properties of MHPs-NCs perovskites through RE doping.

2. Results and discussion

The CsPbBr$_3$ NCs were synthesized via the hot injection method to achieve NCs with homogeneous cubic morphologies.[45] Cs-oleate was injected into the PbBr$_2$ precursor while octadecene (ODE), oleic acid (OA), and oleylamine (OLA) were present. Both *in-situ* and *ex-situ* doping approaches were investigated to attain effective doping of CsPbBr$_3$ with Eu ions. We added three different weight percentages of the Eu dopant in both approaches: 2.5, 5, and 10 wt%. In the *in-situ* doping method, we introduced Eu(NO$_3$)$_3$ into the PbBr$_2$, OA, and OLA precursors. Namely, the Eu dopant was present during the formation of the NCs. Conversely, *ex-situ* doping involves an additional synthetic step following the hot injection process, where undoped CsPbBr$_3$ NCs are dispersed in toluene and sonicated with Eu(NO$_3$)$_3$. It is essential to note that, throughout this paper, the undoped and *ex-situ* doped NCs underwent ultrasonic treatment to ensure a fair comparison. This meticulous approach serves to mitigate any concerns regarding discrepancies between the two, thereby providing the integrity of our findings. Each method offers distinct advantages: *ex-situ* doping enables superior control over the doping level, while *in-situ* doping allows a uniform distribution of dopant ions across the CsPbBr$_3$ NCs.

TEM images of the undoped, *in-situ,* and *ex-situ* Eu-doped CsPbBr$_3$ NCs are shown in **Figure 1A-C** and ***Figure S1*A-D**. Notably, despite changes in size due to doping, the NCs maintain their general cubic shape. To determine the size of the doped and undoped CsPbBr$_3$ NCs, we extracted FFT patterns from the TEM images (see ***Figure S2***), and the results are summarized in **Figure 1D**. We found that for both methods, the size of the doped NCs decreases upon introducing 2.5 wt% of Eu dopant. However, the NCs size rises as the doping level increases. The decrease in the size of the NCs occurs because of the introduction of a small amount of dopant that provides more nucleation sites, thus promoting faster formation of smaller NCs. However, as the doping level increases, the smallest NCs cannot be stabilized because the ligand concentration remains constant.[46,47] Previous studies have shown a direct correlation between particle size and ligand concentration.[48] Consequently, the small nuclei aggregate and produce larger NCs. Our observations indicate a correlation between the particle size and the dopant level, suggesting an alternative pathway to control the size of CsPbBr$_3$ NCs.
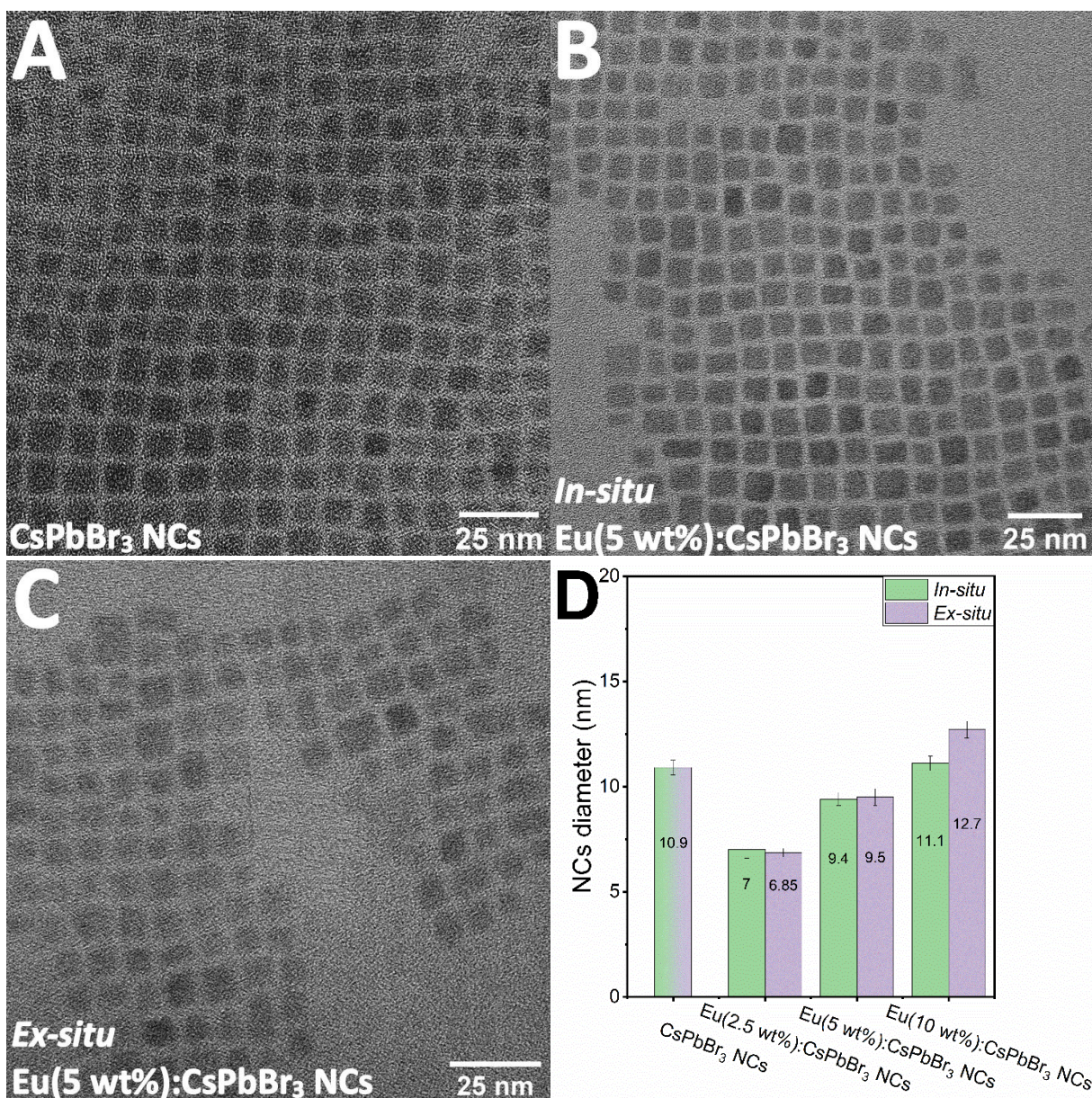
Figure 1: TEM image of (A) CsPbBr3 NCs, (B) in-situ Eu(5 wt%):CsPbBr3 NCs and (C) ex-situ Eu(5 wt%):CsPbBr3 NCs. (D) The average size of the undoped and doped Eu:CsPbBr3 NCs. Here, the error bar indicates the size distribution. Note that Eu(5 wt%):CsPbBr3 NCs refers to the Eu-doped CsPbBr3 NCs, with the value in parentheses indicating the nominal Eu-dopant concentration.

The results of the semi-quantitative EDS analysis for *in-situ* and *ex-situ* Eu ions doped $CsPbBr_3$ NCs are displayed in **Table S1**. The EDS analysis confirms the presence of Br, Cs, and Pb elements in all the examined samples. Notably, the quantitative analysis of the Eu weight percentage (wt%) using the SEM-EDS technique is suboptimal. However, the results from the semi-quantitative analysis of the *in-situ* doped NCs are quite promising. Here, the quantity of Eu ions increases according to the nominal amount introduced during synthesis. Specifically, the measured values of Eu ions are 0.9, 1.0, and 1.5 at% compared to the nominal ones of 2.5, 5, and 10 wt%, respectively. The latter observation indicates that with a low initial dopant concentration, approximately 50% of nominal Eu ions concentration is introduced into the $CsPbBr_3$ lattice. However, as the nominal doping rate increases, the amount of dopant in the NCs

lattice does not grow proportionally. This finding suggests that Eu doping is a self-limiting process, meaning that only a limited amount actually succeeds in integrating into the lattice. For the *ex-situ* samples, the Eu atoms are likely non-uniformly dispersed on the surface of the nanocrystals (NCs), significantly compromising the accuracy of the quantitative data. Consequently, the EDS results for the *ex-situ* Eu ions doped NCs show Eu values of 2.8, 5.8, and 15.5 atomic percent (at%) compared to the nominal values of 2.5, 5, and 10 wt%, respectively.

XRD patterns of doped and undoped $CsPbBr_3$ NCs are present in **Figure 2**. The XRD analysis confirms the presence of $CsPbBr_3$ in an orthorhombic phase for all the examined samples. However, the XRD pattern of the *in-situ* Eu(10 wt%):$CsPbBr_3$ NCs exhibits a combination of the orthorhombic phase and the hexagonal phases of Cs_4PbBr_6 (**Figure 2A**). Conversely, for *ex-situ* Eu(10 wt%):$CsPbBr_3$ NCs, the XRD pattern exhibits a combination of the orthorhombic phase and tetragonal phases of Cs_2PbBr_5 (**Figure 2B**). Thus, we can conclude that, at a high rate, the Eu dopant degrades the $CsPbBr_3$ orthorhombic phase, resulting in the formation of other stoichiometries of Cs, Pb and Br, including Cs_4PbBr_6 and Cs_2PbBr_5.[49]

According to the previous reports, the influence of Eu doping becomes apparent at ~21.5°, the *112* XRD plane.[50] Notably, there is a significant overlap between most of the XRD peaks of $CsEuBr_3$ and those of $CsPbBr_3$ (orthorhombic phase). Thus, the XRD peak between 21°-22° of undoped and doped NCs was deconvolved to classify independent diffraction peaks (see **Figure 2C**). For the undoped $CsPbBr_3$ NCs, we observe the presence of ~21.50°, 21.47°, and 21.64° peaks ascribed to *020*, *112*, and *200* planes, respectively. (JCPDS PDF 01-090-0380) For the *ex-situ* doped $CsPbBr_3$, the deconvolution produced no valuable insights, i.e., the peak position did not change as a result of the doping. (**Figure S3**). This finding suggests that the dopant does not reside within the lattice of $CsPbBr_3$ and is most likely trapped on the surface of the nanocrystals.

Interestingly, in the case of the *in-situ* doped NCs, the deconvolution suggests the emergence of an additional peak at 21.53° for Eu(2.5 and 5 wt%) and ~21.51° for Eu(10 wt%). That peak is characteristic of the *112* XRD plane of $CsEuBr_3$. (JCPDS PDF 04-014-8774) The peak shift for lower Eu ions rate is attributed to the partial replacement of Pb^{2+} with an ionic radius of ($r_{ion} = 119\ pm$) by Eu^{3+} with a smaller radius of $r_{ion} = 94.7\ pm$ and, accordingly, decreased lattice parameters. Hence, the peak shifts to higher angles for Eu:$CsPbBr_3$ NCs[1] due to the distortion caused by introducing the Eu^{3+} dopant into the lattice.[50] Interestingly, the peak shift to lower angles for Eu(10 wt%):$CsPbBr_3$ NCs*****. That shift is induced by the dopant phase segregation in the form of $CsEuBr_3$. The shift in the *112* plane peaks confirms substitutional doping, eliminating the possibility of physical adsorption of Eu^{3+} ions on the surfaces of the prepared NCs.

---

[1] *Note that Eu:CsPbBr₃ NCs refers to the Eu-doped CsPbBr₃ NCs, with the value in parentheses indicating the nominal Eu-dopant concentration.*

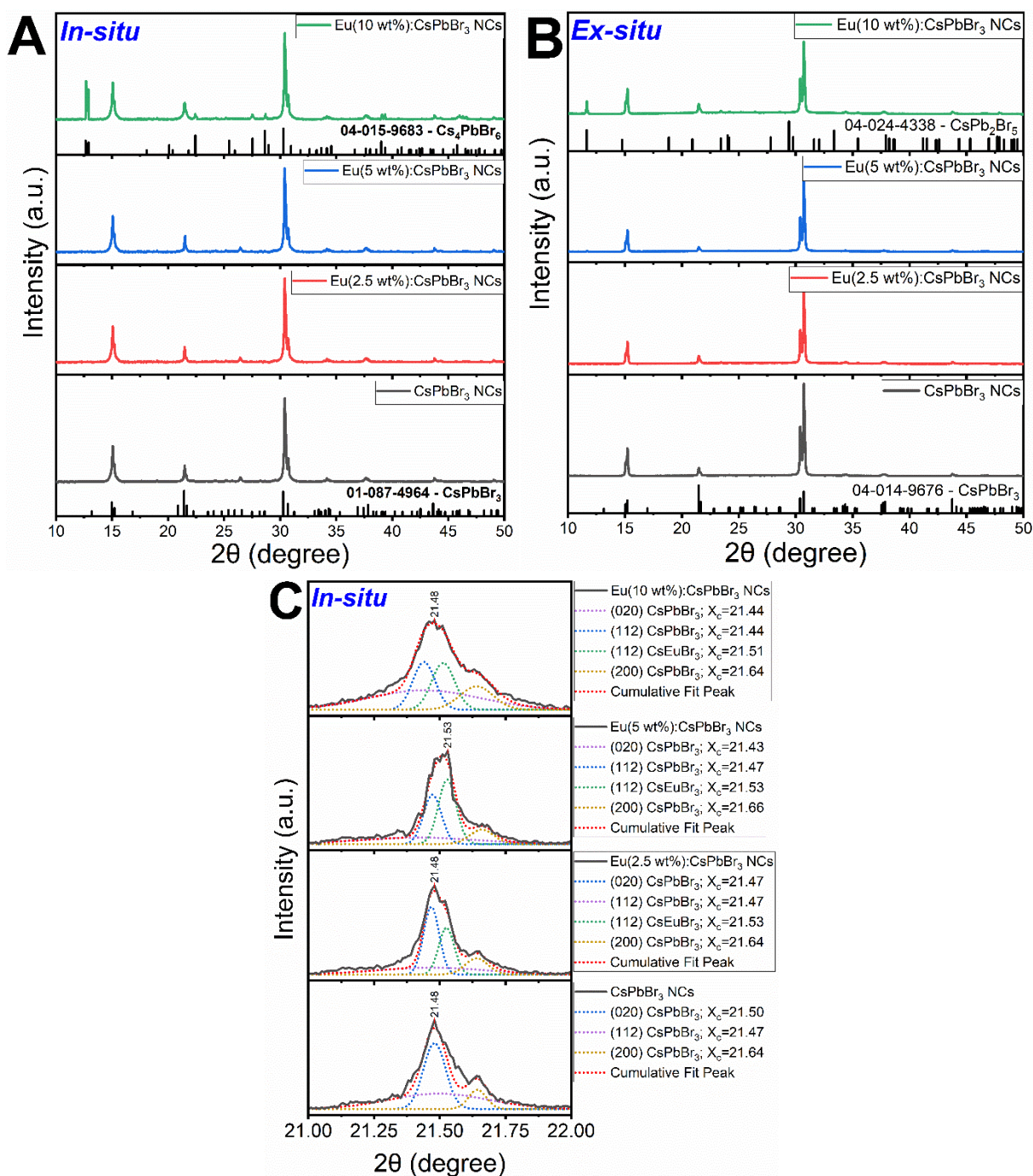**Figure 2**: A - XRD patterns of neat $CsPbBr_3$ NCs and *in-situ* Eu-doped $CsPbBr_3$ NCs with different Eu^{3+} doping. Insert XRD patterns of the orthorhombic phase of $CsPbBr_3$ (JCPDS PDF 04-014-9676) and the hexagonal phase of Cs_4PbBr_6 (JCPDS PDF 04-015-9683). B – XRD patterns of $CsPbBr_3$ *ex-situ* Eu-doped $CsPbBr_3$ NCs with different Eu^{3+} doping. Insert XRD patterns of the orthorhombic phase of $CsPbBr_3$ (JCPDS PDF 96-451-0746) and the Tetragonal phase of Cs_2PbBr_5 (JCPDS PDF 04-024-4338). C- deconvolution of XRD peak 112 of *in-situ* doped and undoped $CsPbBr_3$ NCs.

XPS measurements were used to determine the redox level of the Eu dopant. **Table 1** displayed the XPS measurement for undoped, *in-situ*, and *ex-situ* doped Eu(10 wt%): $CsPbBr_3$ NCs (**Table S2**). The lower doping rate produced unreliable results due to the technique's limitations. Therefore, this section

presents only the XPS results of 10 wt% doped samples. The results showed that both undoped and Eu ions doped NCs contained Cs, Pb, and Br, as evidenced by the peaks corresponding to the Cs 3d (720-740 eV), Pb $4f_{7/2}$ (136-144 eV), and Br $3d_{5/2}$ (66-70 eV) orbitals. Both Eu-doped $CsPbBr_3$ NCs exhibited peaks corresponding to the Eu^{3+} $3d_{5/2}$ orbital. Therefore, the redox level of the Eu ion in the doped $CsPbBr_3$ NCs is 3^+. The intensity of the Eu^{3+} $3d_{5/2}$ orbital is greater in *ex-situ* Eu(10 wt%): $CsPbBr_3$ NCs compared to *in-situ* Eu^{3+}(10 wt%):$CsPbBr_3$ NCs. The results of the XPS measurements confirm that Eu^{3+} resides on the surface of *ex-situ* Eu^{3+}(10 wt%): $CsPbBr_3$ NCs.

Table 1: XPS measurement results for undoped and both *in-situ* and *ex-situ* doped Eu^{3+}(10 wt%): $CsPbBr_3$ NCs.

	Undoped CsPbBr₃ NCs	*In-situ* doped Eu³⁺(10 wt%): CsPbBr₃ NCs	*Ex-situ* doped Eu³⁺(10 wt%): CsPbBr₃ NCs
Cs 3d	10.1	7.31	9.89
Pb 4f	18.09	30.42	18.22
Br 3d	71.81	61.17	68.94
Eu 3d	-	1.1	2.95

The UV-vis absorption spectra of doped and undoped $CsPbBr_3$ NCs are displayed in **Figure 3**. A distinctive absorbance edge at 516 nm is evident in all measured samples, attributed to $CsPbBr_3$ NCs. As observed from **Figure 3A**, for the *in-situ* doped NCs, the absorbance edge is red-shifting to 519 and 524 nm for 2.5 and 5 wt% Eu^{3+} doped NCs, respectively. However, upon increasing the doping level to 10 wt%, the absorbance is blue-shifted to 521 nm. The alteration in the absorbance edge underscores the significant influence of Eu^{3+} doping on the optoelectronic characteristics.[47] This phenomenon has been thoroughly described in previous reports in the field of semiconductor doping.[51] In high Eu^{3+} concentrations, the lattice distortion is too high, resulting in the segregation of the Eu^{3+} in the lattice of $CsPbBr_3$ and a decrease in the effect of doping on the optical properties. Indeed, the XRD results of the Eu(10 wt%):$CsPbBr_3$ NCs presented above support our observation.

The optical bandgaps (E_g) were evaluated from the absorption spectra using the Tauc relation.[52] For the *in-situ* Eu:$CsPbBr_3$ NCs, E_g is shifting from 2.36 to 2.35, 2.29, and 2.34 eV for 0, 2.5, 5, and 10 wt% Eu^{3+}, respectively. This phenomenon results from lattice defects due to the incorporation of the Eu^{3+} dopants into the $CsPbBr_3$ lattice.[53] In addition, the absorption spectra reveal a visible background increase occurring between 525 and 800 nm. The rise is induced by the presence of the Eu^{3+} dopants that create an excess of electrons in the conduction band (CB) of $CsPbBr_3$. Consequently, a new defect band (donor level) is forming below the CB, causing a reduction in the optical bandgap of Eu:$CsPbBr_3$ NCs.[54]

For *ex-situ* doping, the absorbance spectra remain unchanged compared to the undoped $CsPbBr_3$ NCs and exhibit a strong absorbance edge at 511 nm (bandgap of 2.39 eV), **Figure 3B**. As a result, the optical bandgaps for all the NCs are 2.39 eV. This result indicates that the Eu^{3+} does not alter the lattice of $CsPbBr_3$ during the process of *ex-situ* doping, and the dopant atoms reside on the surfaces of the NCs.[55]

The emission spectra of the Eu^{3+}-doped and undoped $CsPbBr_3$ NCs are shown in **Figure 3**. For the *in-situ* doped NCs, the photoluminescence (PL) of Eu(2.5 wt%):$CsPbBr_3$ NCs is similar to that of the undoped NCs with a maximum at 510 nm and FWHM of 21 nm (**Figure 3A**). The emission intensity of Eu(5 wt%):$CsPbBr_3$ NCs is reduced and red-shifted from 510 to 515 nm with a FWHM of 19 nm. The intensity reduction and the maxima red-shift can be rationalized by non-radiative recombination of the photo-excited exciton with the Eu^{3+}-induced carriers[56,57] The decrease in FWHM to 19 nm could be ascribed to a rise in the

concentration of the Eu^{3+}-dopants, which reduces the NCs' defects, thereby enhancing crystallinity and size uniformity.[58] Indeed, the TEM images and size distribution shown in **Figure 1D** clearly demonstrate the uniform size distribution of the NCs. Lastly, the emission intensity of $Eu(10 wt\%):CsPbBr_3$ NCs is further reduced, but it shifts to a shorter wavelength, with a maximum of 512.5 nm and FWHM of 21 nm. The decrease in the emission peak suggests a non-radiative reduction process induced by an excess of dopants.[56] Additionally, the surplus of dopants could introduce more defects, resulting in larger NCs and a broader size distribution, as evidenced by the FWHM of 21 nm.[58]

For the *ex-situ* doping method, the doped and undoped $CsPbBr_3$ NCs exhibit similar emission spectra with a maxima peak at 520 nm and a FWHM of 16 nm. (**Figure 3B**) The main difference lies in the emission intensity. The NCs doped with 2.5 and 5% Eu^{3+} exhibit a slight enhancement in their emission spectra. Nevertheless, there is a noticeable PL quenching for $Eu(10 wt\%):CsPbBr_3$ NCs induced by the non-radiative recombination due to a high defects concentration.[56]

In addition to the prominent PL emission peak, all the examined samples exhibit a shoulder-like maximum at ~619 nm. (**Figure 5C-D** inset) The prominence of this shoulder becomes much more pronounced at an excitation wavelength (λ_{ex}) of 308 nm, while the primary PL peak reaches its maximum intensity at λ_{ex}=320 nm. Moreover, for all the doped NCs, the intensity of this peak is increased. For the undoped $CsPbBr_3$ NCs, this emission shoulder can be assigned to charge transfer from the ligands (i.e., OLA) to the Pb/Cs metal.[59–61] In the doped samples, there is an additional contribution to the shoulder, originating from the $^5D_0 \rightarrow {}^7F_2$ transition of Eu^{3+} ions.[62] This particular transition represents the highest intensity emission of Eu^{3+} ions and is termed a hypersensitive transition due to its responsiveness to the environment.[61,63,64] Therefore, the alteration in the intensity of the 619 nm shoulder can serve as a prominent indicator of successful Eu^{3+} doping and its rate. This radiative electron transition indicates that there is non-equivalence (Eu^{3+} vs. $CsPbBr_3$) of the crystallographic position of the Eu^{3+} ions.[61] Namely, the Eu^{3+} occupies a site overlapping the center of inversion symmetry.[64]

For all the *in-situ* Eu^{3+}-doped $CsPbBr_3$ NCs, the PL intensity of shoulder-like maximum increases by 153% compared to the undoped NCs. (**Figure 3C, inset**) On the contrary, for the *ex-situ* doped NCs, the enhancement observed for doping rates of 2.5 and 5 wt% is only marginal compared to undoped NCs. This observation indicates that the dopant atoms do not reside within the NCs, and thus, Eu^{3+} does not strongly affect the PL intensity. As for the $Eu(10 wt\%):CsPbBr_3$ NCs, the intensity of the shoulder-like maximum at 619 nm increases by 110% compared to the undoped NCs. This observation strongly supports the notion that for *ex-situ* doping, a high initial concentration of the Eu^{3+} dopant will be more successful and can significantly impact the optoelectronic properties of the $CsPbBr_3$ NCs.
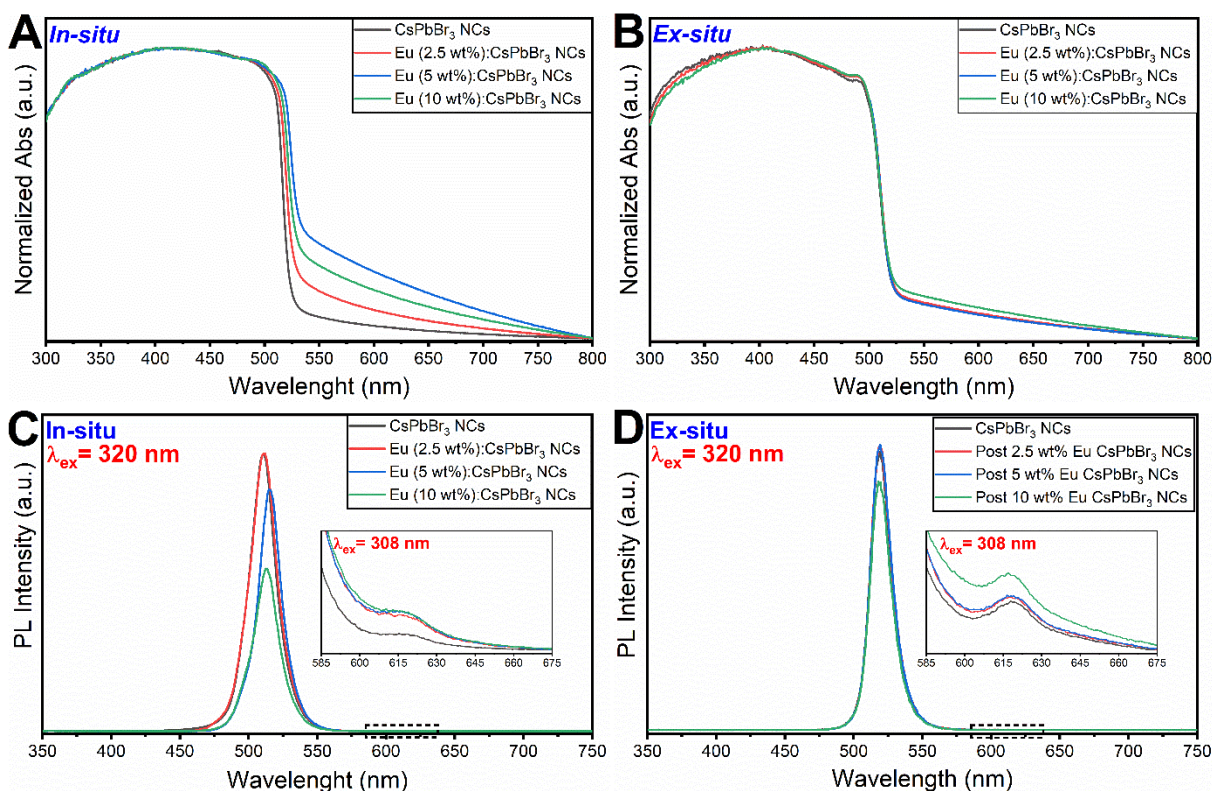
Figure 3: Absorption spectra of Eu^{3+}-doped and undoped $CsPbBr_3$ NCs doped with different dopant ratios via (A) *in-situ* and (B) *ex-situ* doping methods. Emission spectra (λ_{ex} = 320 nm) for Eu^{3+}-doped $CsPbBr_3$ NCs by the (C) *in-situ* and (D) *ex-situ* methods. Inset: Emission spectra (λ_{ex} = 308 nm) of the shoulder-like maxima ascribed to the $^5D_0 \rightarrow {}^7F_2$ transition with a high bandwidth (slit=10 nm).

Our findings indicate that Eu^{3+} doping, in both doping methods, has an observable impact on the structural and optoelectronic properties of the $CsPbBr_3$ NCs. Consequently, we will investigate the effects of these doping methods on their photocatalytic properties. The photocatalytic efficacy of both Eu^{3+}-doped and undoped $CsPbBr_3$ NCs was examined by assessing their capability to degrade methyl orange (MO) dye under visible-light irradiation. This particular azo dye was chosen due to its widespread use in research laboratories, textile manufacturing, printing, and pharmaceutical industries,[65] all of which substantially pollute the environment. **Figure 4A** shows the change in the absorbance of the MO dye at different time intervals for the *in-situ* Eu^{3+}-doped $CsPbBr_3$ NCs, while **Figure S4** shows the results for the *ex-situ* $Eu:CsPbBr_3$ NCs. The reduction of the MO characteristic absorption maxima ($\lambda_{max} \sim 420\ nm$) was used for tracking the progression of the dye degradation. In addition, we assessed the photocatalytic efficiency of all NCs by comparing the degradation rate ($D\%$), and the kinetics of the photocatalytic reactions, as detailed in the methods section.

All the samples exhibit photocatalytic activity toward dye degradation. However, the *in-situ* Eu^{3+}-doped $CsPbBr_3$ NCs are more efficient compared to both the undoped and the *ex-situ* doped NCs. After illumination for 80 min, the MO is 90% degraded using $CsPbBr_3$ NCs. Using the *in-situ* Eu^{3+}-doped NCs, the MO degraded to 95, 98, and 68% when dopant levels of 2.5, 5, and 10 Eu^{3+}-wt.%, respectively. (**Figure 4A**) Comparatively, for the *ex-situ* doped NCs, the degradation rate of the MO is 45, 21, and 20% when using 2.5, 5, and 10 Eu^{3+} wt.% of $Eu:CsPbBr_3$, respectively. (**Figure S4). Namely,** we found that the *in-situ doped*

Eu(5 wt%):CsPbBr$_3$ NCs exhibited the fastest degradation rate. A zero-order kinetic model of the photocatalytic process provided the best fit for the experimental results. The derived degradation and reaction rate constants are presented in **Table 2** and **Figure S5**.

Generally, we found that the *in-situ* Eu^{3+}-doped NCs demonstrated enhanced photocatalytic efficiency compared to their *ex-situ* counterparts. The poor performance of the e*x-situ* doped NCs can be explained by the positions of Eu^{3+}, i.e., on the surface and not within the CsPbBr$_3$ lattice. Namely, the Eu^{3+} ions mainly reside at the periphery of the NCs, leading to limited or detrimental effects on photocatalytic performance due to inefficient charge transfer.[66] Interestingly, when the Eu^{3+} doping rate reaches 10wt%, the photocatalytic properties deteriorate for both *ex-situ* and *in-situ* Eu^{3+}-doped NCs. This phenomenon is possibly explained by the segregation of the Eu^{3+} phase, which can be seen in the XRD results. The investigation into the photocatalytic performance underlines the significant influence of Eu^{3+} doping on the attributes of CsPbBr$_3$ NCs.

Table 2: Rate constant (k$_0$) of *in-situ* and *ex-situ* Eu^{3+}-doped CsPbBr$_3$ NCs.

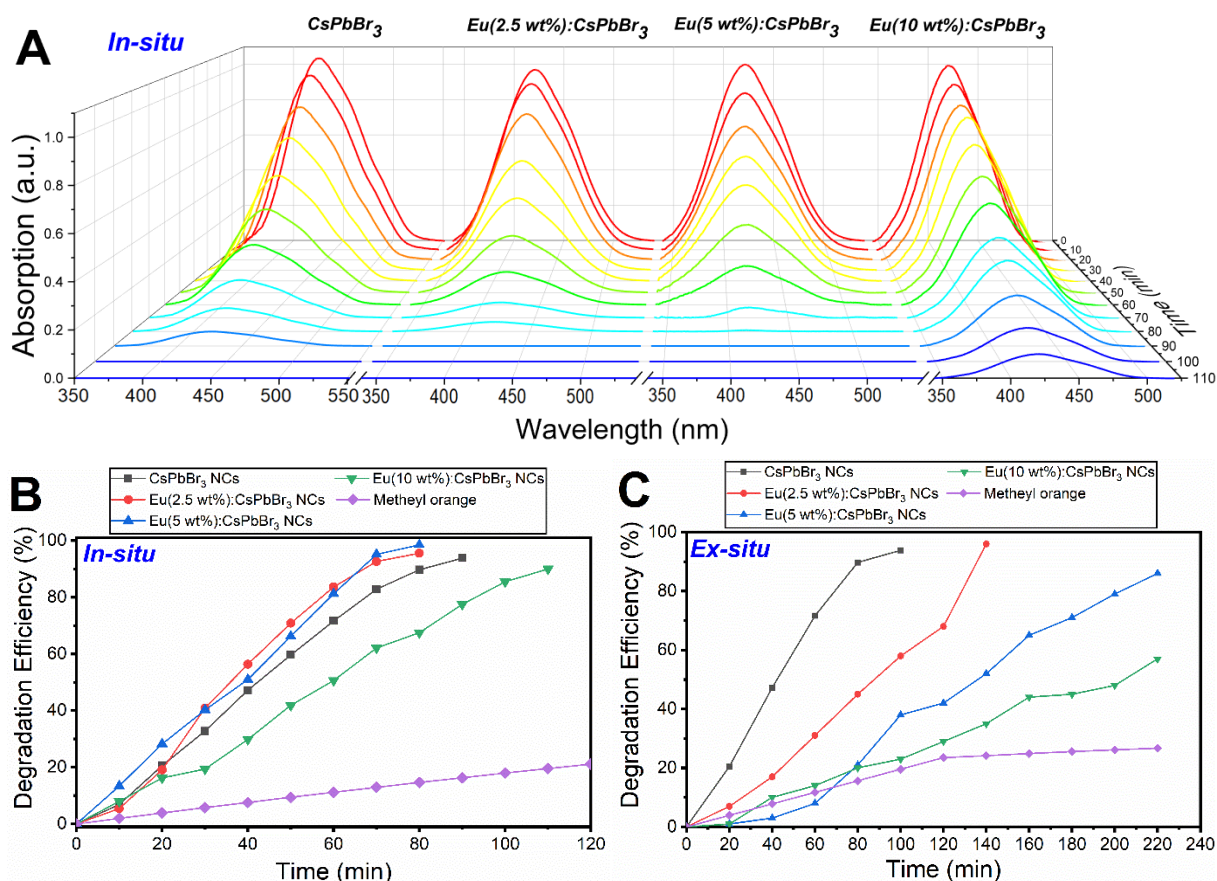|	*In-situ* Eu^{3+}-doped CsPbBr$_3$ NCs	*Ex-situ* Eu^{3+}-doped CsPbBr$_3$ NCs
CsPbBr$_3$ NCs	-0.0117	-0.0117
Eu(2.5 wt%):CsPbBr$_3$ NCs	-0.0130	-0.0067
Eu(5 wt%):CsPbBr$_3$ NCs	-0.0129	-0.0044
Eu(10 wt%):CsPbBr$_3$ NCs	-0.0086	-0.0027

Figure 4: (A) 3D UV-visible spectra of MO photodegradation after different light irradiation times using CsPbBr$_3$ NCs and *in-situ* Eu^{3+}-doped CsPbBr$_3$ NCs. Photodegradation efficiency of methyl orange (MO) under light illumination is presented for (B) *in-situ* Eu^{3+}-doped CsPbBr$_3$ NCs and (C) *ex-situ* Eu^{3+}-doped CsPbBr$_3$ NCs with varying weight percentages.

The photocatalytic dye degradation is known to be initiated by the radicals provided by the catalyst. Hence, to further understand the impact of Eu^{3+} doping on photocatalytic performance, we examine the doped and undoped CsPbBr$_3$ NCs using electron paramagnetic resonance (EPR) analysis, **Figure 5**. The EPR analysis allows us to follow the radical formation and identify them. To initiate the radical formation, we excite the NCs with the visible light with the presence of an organic molecule known as a "spin trap". The "spin trap" can detect the short-leaved radical species and stabilize their formation. We used 5-tert-butoxycarbonyl-5-methyl-1-pyrroline-N-oxide (BMPO) as a trapping agent, which prevents the radical from decaying into a hydroxyl adduct in addition to the ability to prolong the radical's lifetime.
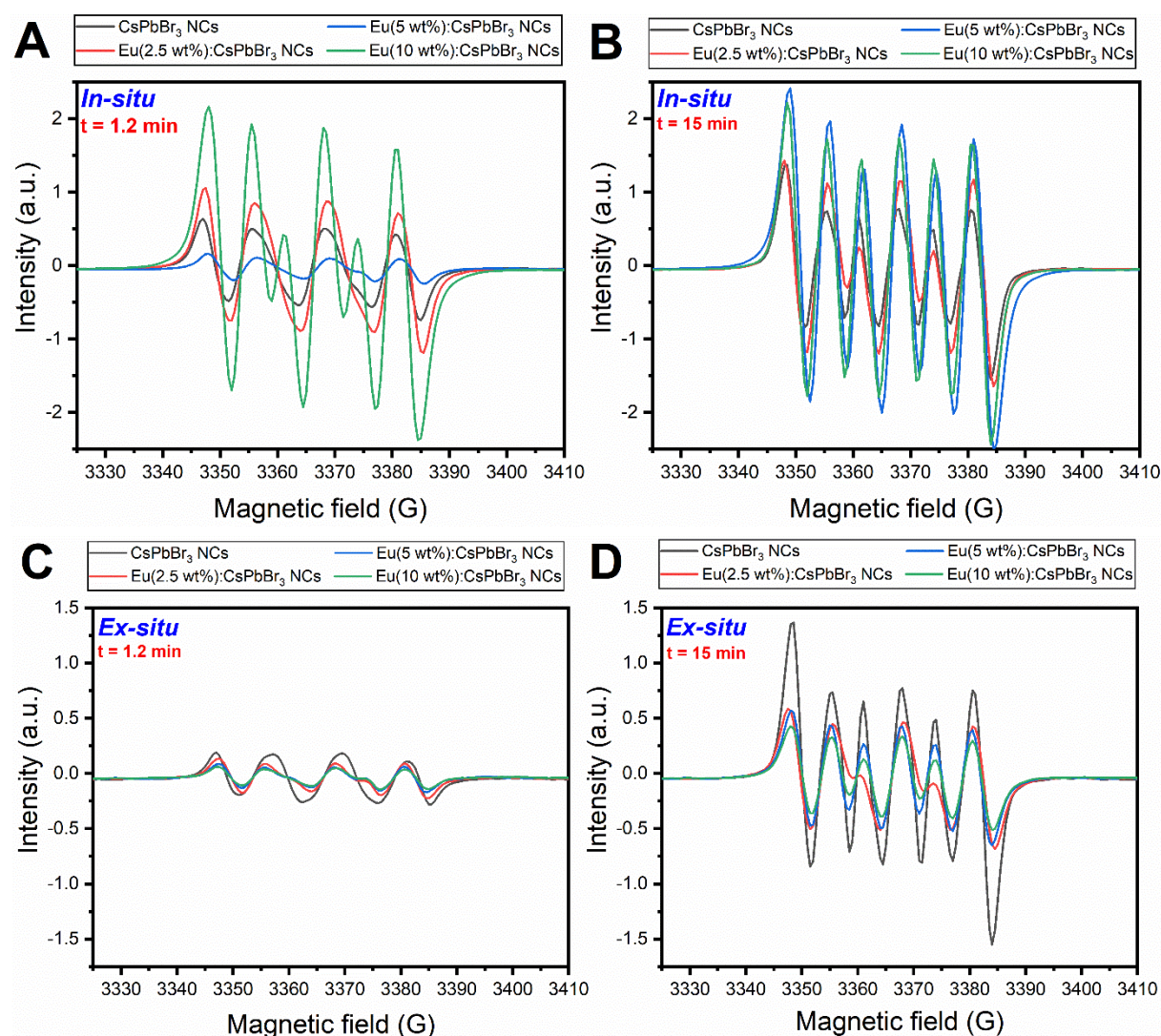

Figure 5: EPR results comparing *in-situ* and *ex-situ* Eu^{3+}-doped CsPbBr$_3$ NCs with varying Eu^{3+} doping (in wt%) are presented under light illumination for 1.2 min (A and C) and 15 min (B and D).

In the dark, a minimal signal was observed, probably resulting from the ultrasonic treatment used to mix the reactants, which is known to generate free radicals in solutions. Then, after 1.2 minutes of visible light irradiation, almost all the samples except 10% Eu^{3+} gave an EPR spectrum of BMPO spin trap centered around g = 2 and exhibited four lines, typical for a reaction with hydroxyl radicals ($\cdot OH^-$)[67] (**Figure 5A** and **Figure 5C**). The EPR spectrum of the sample with 10% Eu^{3+} with BMPO consisted of six lines, typical for reaction with superoxide radicals ($\bullet O_2{}^-$).[68]

For CsPbBr$_3$ NCs, the intensity increased with time and split into six peaks, indicative of the production of superoxide $\bullet O_2{}^-$ radicals (**Figure 5B**). The broad spectra observed at short illumination times suggest a mixture of superoxide and hydroxyl radicals. Over longer times, the evolution of the superoxide spectra indicates that the initial superoxide radicals are being converted into hydroxyl radicals. The $\bullet O_2{}^-$ is generated by the oxidation of CsPbBr$_3$ NCs, could either react to produce $H_2O_2 + O_2$ or react with $BMPO$ to form a $BMPO \bullet O_2{}^-$. The same phenomena occur for *in-situ* Eu(5 wt%):CsPbBr$_3$ NCs and *ex-situ* Eu^{3+}-doped, see **Figure 5B** and **Figure 5D**. However, for *in-situ* Eu(10 wt%):CsPbBr$_3$ NCs, the intensity started very high and stable for a longer time ($t = 1.2 - 15\ min$), even when they split into six peaks. The initial intensity of *in-situ* Eu^{3+}-doped CsPbBr$_3$ NCs is much higher and faster compared to *ex-situ* counterparts. Therefore, the *in-situ* Eu^{3+}-doped CsPbBr$_3$ NCs produce more radicals compared to their *ex-situ* counterparts. These results confirm the successful incorporation and distribution of the Eu^{3+} dopant in the host CsPbBr$_3$ lattice in the *in-situ* doped compared to the *ex-situ* doped.

3. Conclusions

In conclusion, a comprehensive study on the effects of *in-situ* and *ex-situ* Eu^{3+}-doping of CsPbBr$_3$ NCs was undertaken. The results provide valuable insights into the structural and optical modifications induced by the incorporation of Eu^{3+} ions in the NCs lattice (*in-situ* doping) and on its surface (*ex-situ* doping). The confirmation of Eu^{3+} doping through various analyses, including TEM, XRD, absorbance spectroscopy, and PL emission, underscores the effectiveness of both Eu doping methods. Notably, *in-situ* Eu^{3+}-doped, particularly with Eu(5 wt%):CsPbBr$_3$, has a more pronounced impact on the structural and optical properties compared to *ex-situ* Eu^{3+} doping. The XRD results indicate that the *in-situ* Eu^{3+}-doped CsPbBr$_3$ NCs are incorporated into the lattice of the orthorhombic phase. The Eu^{3+} ions lead to decreased lattice parameters owing to the smaller ion radius of Eu^{3+} ion. The absorbance spectrum of the *in-situ* Eu doping is red-shifts with increasing Eu^{3+} concentration up to Eu(5 wt%):CsPbBr$_3$ and blue-shifts at Eu(10 wt%):CsPbBr$_3$ NCs. The *ex-situ* Eu^{3+} doping shows no significant absorbance change. The emission spectra of the *in-situ* doped NCs reveal quenching, red-shifting, and a growing shoulder peak at 619 nm with increasing Eu^{3+} concentration. The *ex-situ* Eu^{3+} doping results in a slight enhancement for 2.5 and 5 wt% Eu^{3+} and clear PL quenching at 10 wt%, with a consistent peak at 520 nm, indicating the distinct influence of Eu^{3+} doping on emission characteristics. The photocatalytic activity of Eu^{3+}-doped CsPbBr$_3$ NCs exhibited higher degradation efficiency and faster kinetics in the presence of *in-situ* Eu^{3+}-doped CsPbBr$_3$ NCs compared to their *ex-situ* counterparts. Specifically, after 80 minutes of illumination, *in-situ* Eu^{3+} doping with Eu^{3+} (5 wt%):CsPbBr$_3$ NCs achieved 98% MO degradation. Overall, this study contributes to a comprehensive understanding of the nuanced effects of Eu^{3+} doping on the structural, optical, and photocatalytic properties of CsPbBr$_3$ NCs, providing valuable information for potential applications in optoelectronic devices and catalysis.

4. Experimental section

4.1. Methods:

Preparation of Cs-Oleate Stock Solution: 81.4 mg Cs_2CO_3 (Alfa Aesar, 99.9%) with 4 mL octadecene (ODE, Sigma-Aldrich, 90%) and 0.25 mL oleic acid (OA, Sigma Aldrich, 90%) were loaded into a vial and dried under vacuum for one h at 120 °C. Then, the mixture was heated under an N_2 atmosphere for one hour at 150 °C until the OA dissolved all the Cs_2CO_3, and the solution turned clear yellow.

Preparation of Pb-Oleate Stock Solution: 69 mg $PbBr_2$ (Alfa Aesar, 99.9%) with 0.5mL OA, 0.5mL oleylamine (OLA, Thermo Scientific Chemicals, 80-90%) and 5 mL ODE were loaded into a three-neck flask.

Synthesis of $CsPbBr_3$ NCs: Pb precursor was degassed for one hour at 120 °C. After $PbBr_2$ was completely dissolved, the temperature was raised to 140 °C for one hour under N_2 atmosphere. Then, 0.4 mL of Cs-oleate precursor was quickly injected into the Pb precursor. After 30 s of stirring, an ice-water bath cooled the reaction mixture immediately. The crude solution was centrifuged at 11000 rpm for 10 min, and the precipitate was collected and redispersed in 4 mL toluene for further characterization.

Synthesis of in-situ Eu‑doped $CsPbBr_3$ NCs: The Eu-doped $CsPbBr_3$ NCs synthesis is similar to the synthesis of pure $CsPbBr_3$ NCs, as described in section 2.1. The only difference was the addition of 1.7, 3.5, or 6.9 mg $Eu(NO_3)_3$ (corresponding to mass concentrations of 2.5, 5, and 10 wt%) to the Pb precursor.

Synthesis of ex-situ Eu‑doped $CsPbBr_3$ NCs: 50 mg of $Eu(NO_3)_3$ were dissolved in 2 mL toluene. $CsPbBr_3$ NCs dispersion in toluene was synthesized as described in section 2.1 and divided into four tubes. Three different amounts of Eu-toluene solution (corresponding to mass concentrations of 2.5, 5, and 10 wt%) were added to each tube, while one tube was kept Eu-free and was used as a reference. The four tubes were sonicated for 60 min with ice to maintain a constant temperature.

4.2. Characterization Techniques

Transmission electron microscopy (TEM) analysis of the $CsPbBr_3$ NCs was performed using Talos Arctica G3 S/TEM microscope (Thermo Fisher Scientific, USA) with an accelerating voltage of 200kV, X-FEG Electron source. An energy-dispersive X-ray spectroscopy (EDS) detector (super-X EDS system) was attached to the TEM instrument, which allowed the chemical composition of the nanocrystals to be determined. The samples were prepared by dropping 5 μL of a highly diluted sample solution in hexane onto a copper grid covered by formvar carbon.

X-ray diffraction (XRD) patterns of the $CsPbBr_3$ NCs were collected in a step–scan mode at room temperature using Rigaku SmartLab SE diffractometer with 40 kV X-ray generator (Cu Kα radiation, 10–50° 2θ range, step width 0.03°). The XRD data was analyzed with the assistance of MDI Jade 8.8 software.

X-ray Photoelectron Spectroscopy (XPS) measurements of the $CsPbBr_3$ NCs were performed using a Thermo Scientific ESCALAB QXi. The samples were irradiated with a monochromatic Al Kα radiation.

UV-Vis Spectrophotometer: The absorbance spectra of the $CsPbBr_3$ NCs were recorded in the range of 300-800 nm using a V-750 UV-visible spectrophotometer (Jasco, Japan).

Spectrofluorometer: The photoluminescence (PL) spectra of the $CsPbBr_3$ NCs were recorded using FP-8350 Spectrofluorometer (Jasco, Japan). Here, lasers with 308 nm and 320 nm wavelengths were used for excitation, and the PL was measured in the range 450-650 nm using FP-8350 Spectrofluorometer (Jasco, Japan).

Photocatalysis

Dye degradation was performed to study the photocatalytic activity of the doped and undoped CsPbBr$_3$ NCs. A stock solution was prepared by dispersing 2.5 mg of methyl orange (MO) dye in 10 mL ethanol and 40 mL toluene. For each sample, 15 mL of MO stock solution was added to 20 ml toluene of the CsPbBr$_3$ NCs. Each sample was placed in front of a solar simulator 10500 model (1 sun, Abet-technologies, USA) at a 15 cm distance. 2.5 ml of sample was collected every 10 minutes and centrifuged at 11000 rpm for 1 minute before measuring the absorption spectrum. The degradation rate ($D\%$) was calculated using **Equation 1** and **Equation 2**, where, C_0 and C_t is the dye concentration at $t = 0\ min$ (initial concentration) and $t = t\ min$, respectively.

Equation 1: $D\% = \left(1 - \frac{C_t}{C_0}\right) x100\%$

The zero-order kinetic equation is given by:

$\quad$ **Equation 2** : $C_t = k_0 t + C_0$

Here, k_0 (min^{-1}) is represents the reaction rate constant derived from the slope of the C$_t$ versus time (t) plot.

Electron Paramagnetic Resonance (EPR) spectra of the CsPbBr$_3$ NCs were recorded on a Bruker ELEXSYS 500 X-band spectrometer equipped with a Bruker ER4119HS resonator operating at a microwave frequency of 9.5 GHz. The EPR device operated at a microwave frequency of 100 kHz. Spectra were recorded using a microwave power of 20 mW with a sweeping range of 200 mT and modulation amplitude of 0.1 mT. A stock solution was prepared by sonication of 25 mg 5-tert-butoxycarbonyl-5-methyl-1-pyrroline-N-oxide (BMPO) spin trap in 3.7 mL hexane and 1.25 mL ethanol. Each sample consisted of a 33 µL dispersed solution with CsPbBr$_3$ NCs or CsPbBr$_3$ perovskites with different Eu^{3+} doping levels in hexane, with the addition of 33 µL hexane, 33 µL ethanol, and 100 µL BMPO stock solution. Each sample was inserted into a flat cell Suprasil for aqueous solutions (WG-808-Q, Wilmad) at room temperature.

5. References

1.   Zhou, Y., Chen, J., Bakr, O. M. & Sun, H. T. Metal-Doped Lead Halide Perovskites: Synthesis, Properties, and Optoelectronic Applications. *Chem. Mater.* **30**, 6589–6613 (2018).

2.   Kovalenko, M. V., Protesescu, L. & Bodnarchuk, M. I. Properties and potential optoelectronic applications of lead halide perovskite nanocrystals. *Science (80-.).* **358**, 745–750 (2017).

3.   Zhao, Y. & Zhu, K. Organic-inorganic hybrid lead halide perovskites for optoelectronic and electronic applications. *Chem. Soc. Rev.* **45**, 655–689 (2016).

4. Zhang, H., Nazeeruddin, M. K. & Choy, W. C. H. Perovskite Photovoltaics: The Significant Role of Ligands in Film Formation, Passivation, and Stability. *Adv. Mater.* **31**, 1–29 (2019).

5. Wang, N. *et al.* Perovskite light-emitting diodes based on solution- processed self-organized multiple quantum wells. **10**, (2016).

6. Cao, Y. *et al.* Perovskite light-emitting diodes based on spontaneously formed submicrometre-scale structures. *Nature* (2018) doi:10.1038/s41586-018-0576-2.

7. Xiao, Z. *et al.* Efficient perovskite light-emitting diodes featuring nanometre-sized crystallites. **11**, (2017).

8. Zhang, L. *et al.* Triflate-Passivated Perovskite Colloidal Nanocrystals with Enhanced Emission Performance for Wide-Color-Gamut Backlight Display. *ACS Appl. Nano Mater.* **5**, 12935–12942 (2022).

9. Hoefler, S. F. & Trimmel, G. Progress on lead-free metal halide perovskites for photovoltaic applications : a review. *Monatshefte für Chemie - Chem. Mon.* **148**, 795–826 (2017).

10. Stranks, S. D. & Snaith, H. J. Metal-halide perovskites for photovoltaic and light-emitting devices. *Nat. Publ. Gr.* **10**, 391–402 (2015).

11. Liao, C., Mahmud, A. & Ho-baillie, A. W. Y. Recent progress in layered metal halide. **3**, 4219–4235 (2023).

12. Schröder, V. R. F. *et al.* Using Combinatorial Inkjet Printing for Synthesis and Deposition of Metal Halide Perovskites in Wavelength- Selective Photodetectors. **2101111**, 1–7 (2022).

13.   Kim, J. S. *et al.* Ultra-bright , efficient and stable perovskite light-emitting diodes. **611**, (2022).

14.   Han, B. *et al.* Green Perovskite Light-Emitting Diodes with 200 Hours Stability and 16% Efficiency: Cross-Linking Strategy and Mechanism. *Adv. Funct. Mater.* **31**, 2011003 (2021).

15.   Lei, L., Dong, Q., Gundogdu, K. & So, F. Metal Halide Perovskites for Laser Applications. **2010144**, 1–21 (2021).

16.   Liu, A. *et al.* Metal Halide Perovskites toward Electrically Pumped Lasers. **2200189**, (2022).

17.   Electrocatalysis, S. *et al.* Solar-to-Chemical Fuel Conversion via Metal Halide Perovskite Solar-Driven Electrocatalysis. (2022) doi:10.1021/acs.jpclett.1c03668.

18.   He, Y., Hadar, I. & Kanatzidis, M. G. Detecting ionizing radiation using halide perovskite semiconductors processed through solution and alternative methods. *Nat. Photonics* **16**, 14–26 (2022).

19.   Sarkar, S. All-Inorganic Halide Perovskite Nanocrystals: Future Prospects and Challenges to Go Lead Free. *Phys. Status Solidi Appl. Mater. Sci.* **218**, (2021).

20.   Wu, J. *et al.* Preparation of Eu^{3+}-doped $CsPbBr_3$ quantum-dot microcrystals and their luminescence properties. *Opt. Mater. (Amst).* **97**, 109454 (2019).

21.   Karunakaran, S. K. *et al.* Europium (II)-Doped All-Inorganic $CsPbBr_3$ Perovskite Solar Cells with Carbon Electrodes. *Sol. RRL* **2000390**, 1–8 (2020).

22.   Ding, L. *et al.* Stable Zn-doped $CsPbBr_3$ NCs glasses toward an enhanced optical

performance for WLED. *Ceram. Int.* **45**, 22699–22706 (2019).

23.   Skurlov, I. D. *et al.* Improved one-and multiple-photon excited photoluminescence from
      Cd^{2+}-doped $CsPbBr_3$ perovskite ncs. *Nanomaterials* **12**, 1–16 (2022).

24.   Guo, Y. J. *et al.* Improved Doping and Optoelectronic Properties of Zn-Doped $CsPbBr_3$
      Perovskite through Mn Codoping Approach. *J. Phys. Chem. Lett.* **12**, 3393–3400 (2021).

25.   Yin, J., Ahmed, G. H., Bakr, O. M., Brédas, J. L. & Mohammed, O. F. Unlocking the Effect of
      Trivalent Metal Doping in All-Inorganic $CsPbBr_3$ Perovskite. *ACS Energy Lett.* **4**, 789–795
      (2019).

26.   Yang, D. & Huo, D. Cation doping and strain engineering of $CsPbBr_3$-based perovskite light
      emitting diodes. *J. Mater. Chem. C* **8**, 6640–6653 (2020).

27.   Begum, R. *et al.* Engineering interfacial charge transfer in $CsPbBr_3$ perovskite nanocrystals
      by heterovalent doping. *J. Am. Chem. Soc.* **139**, 731–737 (2017).

28.   Zheng, B. *et al.* Rare-Earth Doping in Nanostructured Inorganic Materials. *Chem. Rev.* **122**,
      5519–5603 (2022).

29.   Malta, O. L. Mechanisms of non-radiative energy transfer involving lanthanide ions
      revisited. *J. Non. Cryst. Solids* **354**, 4770–4776 (2008).

30.   Steblevskaya, N. I., Belobeletskaya, M. V., Ustinov, A. Y. & Medkov, M. A. Synthesis and
      Luminescent Properties of Europium(III, II) Phosphates. *Russ. J. Inorg. Chem.* **64**, 179–184
      (2019).

31. Bala, A. & Kumar, V. Stability of the Eu^{2+} Dopant in $CsPbBr_{3+}$ Perovskites: A First-Principles Study. *J. Phys. Chem. C* **123**, 6965–6969 (2019).

32. Zhang, Y., Zhao, T. & Chen, G. Recent progress in lanthanide ions doped inorganic metal halide perovskites. *J. Rare Earths* **3**, (2023).

33. Pan, G. *et al.* Doping Lanthanide into Perovskite Nanocrystals: Highly Improved and Expanded Optical Properties. *Nano Lett.* **17**, 8005–8011 (2017).

34. Alam, F. *et al.* Eu^{2+}: A suitable substituent for Pb^{2+} in $CsPbX_3$ perovskite nanocrystals? *J. Chem. Phys.* **151**, (2019).

35. Huang, J. *et al.* Lead-free cesium europium halide perovskite nanocrystals. *Nano Lett.* **20**, 3734–3739 (2020).

36. Hesse, S. *et al.* $CsEuBr_3$: Crystal structure and its role in the photostimulation of $CsBr:Eu^{2+}$. *J. Appl. Phys.* **100**, 3–8 (2006).

37. Liu, M. *et al.* In-situ N-doped $MnCO_3$ anode material via one-step solvothermal synthesis: Doping mechanisms and enhanced electrochemical performances. *Chem. Eng. J.* **383**, 123161 (2020).

38. Sumanth Dongre, S., Shwetharani, R., Moyez, S. A. & Balakrishna, R. G. In-situ neodymium ion doping into perovskite nanocrystals over ex-situ and its importance in triclosan sensing. *Mater. Chem. Phys.* **307**, 128221 (2023).

39. Wang, L. *et al.* Surface Reconstruction of Ni-Rich Layered Cathodes: In Situ Doping versus

Ex Situ Doping. *Small Struct.* **3**, (2022).

40. Li, D. B. *et al.* Low-temperature and effective ex situ group V doping for efficient polycrystalline CdSeTe solar cells. *Nat. Energy* **6**, 715–722 (2021).

41. Chen, Y., Liu, Y. & Hong, M. Cation-doping matters in caesium lead halide perovskite nanocrystals: From physicochemical fundamentals to optoelectronic applications. *Nanoscale* **12**, 12228–12248 (2020).

42. van der Stam, W. *et al.* Highly Emissive Divalent-Ion-Doped Colloidal $CsPb_{1-x}M_xBr_3$ Perovskite Nanocrystals through Cation Exchange. *J. Am. Chem. Soc.* **139**, 4087–4097 (2017).

43. Mondal, N., De, A. & Samanta, A. Achieving Near-Unity Photoluminescence Efficiency for Blue-Violet-Emitting Perovskite Nanocrystals. *ACS Energy Lett.* **4**, 32–39 (2019).

44. Di Stasio, F., Christodoulou, S., Huo, N. & Konstantatos, G. Near-Unity Photoluminescence Quantum Yield in $CsPbBr_3$ Nanocrystal Solid-State Films via Postsynthesis Treatment with Lead Bromide. *Chem. Mater.* **29**, 7663–7667 (2017).

45. Protesescu, L. *et al.* Nanocrystals of Cesium Lead Halide Perovskites ($CsPbX_3$, X = Cl, Br, and I): Novel Optoelectronic Materials Showing Bright Emission with Wide Color Gamut. *Nano Lett.* **15**, 3692–3696 (2015).

46. Udayabhaskararao, T., Kazes, M., Houben, L., Lin, H. & Oron, D. Nucleation, Growth, and Structural Transformations of Perovskite Nanocrystals. *Chem. Mater.* **29**, 1302–1308 (2017).

47. Adeleye, A. S., Pokhrel, S., Mädler, L. & Keller, A. A. Influence of nanoparticle doping on the colloidal stability and toxicity of copper oxide nanoparticles in synthetic and natural waters. *Water Res.* **132**, 12–22 (2018).

48. Lu, C. *et al.* Cesium Oleate Precursor Preparation for Lead Halide Perovskite Nanocrystal Synthesis: The Influence of Excess Oleic Acid on Achieving Solubility, Conversion, and Reproducibility. *Chem. Mater.* **31**, 62–67 (2019).

49. Rosentsveig, R. *et al.* Doping of Fullerene-Like MoS_2 Nanoparticles with Minute Amounts of Niobium. *Part. Part. Syst. Charact.* **35**, (2018).

50. Hu, Q. *et al.* Rare Earth Ion-Doped $CsPbBr_3$ Nanocrystals. *Adv. Opt. Mater.* **6**, 1–5 (2018).

51. E. Fred Schubert. *No Doping in III-V Semiconductors*. (2015).

52. Mir, F. A. Transparent wide band gap crystals follow indirect allowed transition and bipolaron hopping mechanism. *Results Phys.* **4**, 103–104 (2014).

53. Ca, N. X. *et al.* Controlling the optical and magnetic properties of CdTeSe and Gd-doped CdTeSe alloy semiconductor nanocrystals. *RSC Adv.* **13**, 36455–36466 (2023).

54. Tan, P. M. *et al.* Study of optical properties and energy transfer mechanism of Tb^{3+}, Sm^{3+} singly doped and co-doped ZnS quantum dots. *Opt. Mater. (Amst).* **114**, 1–9 (2021).

55. Hughes, K. E., Hartstein, K. H. & Gamelin, D. R. Photodoping and Transient Spectroscopies of Copper-Doped CdSe/CdS Nanocrystals. *ACS Nano* **12**, 718–728 (2018).

56. Chen, J. *et al.* Study on luminescence quenching of ultra-small silicon nanocrystals due to

boron doping. *Opt. Mater. Express* **12**, 4096 (2022).

57.   Maibam, B., Baruah, S. & Kumar, S. Photoluminescence and intrinsic ferromagnetism of Fe
       doped zinc oxide. *SN Appl. Sci.* **2**, 1–11 (2020).

58.   Chen, M. *et al.* Strongly Coupled Tin-Halide Perovskites to Modulate Light Emission:
       Tunable 550–640 nm Light Emission (FWHM 36–80 nm) with a Quantum Yield of up to
       6.4%. *Adv. Mater.* **30**, (2018).

59.   Nanowires, M. *et al.* Simultaneous Triplet Exciton − Phonon and Exciton − Photon
       Simultaneous Triplet Exciton − Phonon and Exciton − Photon Photoluminescence in the
       Individual Weak Con fi nement $CsPbBr_3$ Micro / Nanowires. *J. Phys. Chem. C* **123**, 25349–
       25358 (2019).

60.   Khurana, S., Hassan, M. S., Yadav, P., Ghosh, D. & Sapra, S. Impact of Bifunctional Ligands
       on Charge Transfer Kinetics in $CsPbBr_3$-CdSe/CdS/ZnS Nanohybrids. *J. Phys. Chem. Lett.* **13**,
       2591–2599 (2022).

61.   Pustovarov, V. A., Vasin, A. A. & Zuev, M. G. Site-selective luminescence of Eu^{3+} ions in
       silicate-tungstates with apatite and scheelite structures. *Opt. Mater. X* **15**, 100186 (2022).

62.   Feng, P. *et al.* Highly Stable Perovskite Quantum Dots Modified by Europium Complex for
       Dual-Responsive Optical Encoding. *ACS Nano* **15**, 6266–6275 (2021).

63.   Nair, G. B. & Dhoble, S. J. Photoluminescence properties of Eu^{3+}/ Sm^{3+} activated
       $CaZr_4(PO_4)_6$ phosphors. *J. Fluoresc.* **26**, 1865–1873 (2016).

64. Yawalkar, M. M., Zade, G. D., Dabre, K. V. & Dhoble, S. J. Luminescence study of Eu^{3+} doped $Li_6Y(BO_3)_3$ phosphor for solid-state lighting. *Luminescence* **31**, 1037–1042 (2016).

65. Channei, D. *et al.* Photocatalytic degradation of methyl orange by CeO_2 and Fe-doped CeO_2 films under visible light irradiation. *Sci. Rep.* **4**, (2014).

66. Mansuroglu, D. & Umit Uzun-Kaymak, I. Investigation into Ex-Situ and In-Situ Iodine Doped Plasma Polymerized Fluorene-type Thin Films. *Mater. Today Proc.* **18**, 1955–1963 (2019).

67. Zang, L. Y. & Misra, H. P. EPR kinetic studies of superoxide radicals generated during the autoxidation of 1-methyl-4-phenyl-2,3-dihydropyridinium, a bioactivated intermediate of Parkinsonian-inducing neurotoxin 1-methyl-4-phenyl-1,2,3,6-tetrahydropyridine. *J. Biol. Chem.* **267**, 23601–23608 (1992).

68. Polovka, M., Brezová, V. & Staško, A. Antioxidant properties of tea investigated by EPR spectroscopy. *Biophys. Chem.* **106**, 39–56 (2003).

Europium Doping Effects on the Properties of CsPbBr₃ Nanocrystals: *In-situ* vs. *Ex-situ* Synthetic Path Analysis

Hila Shalom[1], Raanan Carmieli[2], Pini Shekhter[3], Lena Yadgarov[1,*]

4. Department of Chemical Engineering, Ariel University, Ariel, 4076414, Israel;
5. Department of Chemical Research Support, Weizmann Institute of Science, Rehovot 7610001, Israel;
6. Center for Nanoscience and Nanotechnology, Tel-Aviv University, Ramat Aviv, Tel Aviv 6997801, Israel;
Email: lenay@ariel.ac.il.

3. Results and discussion
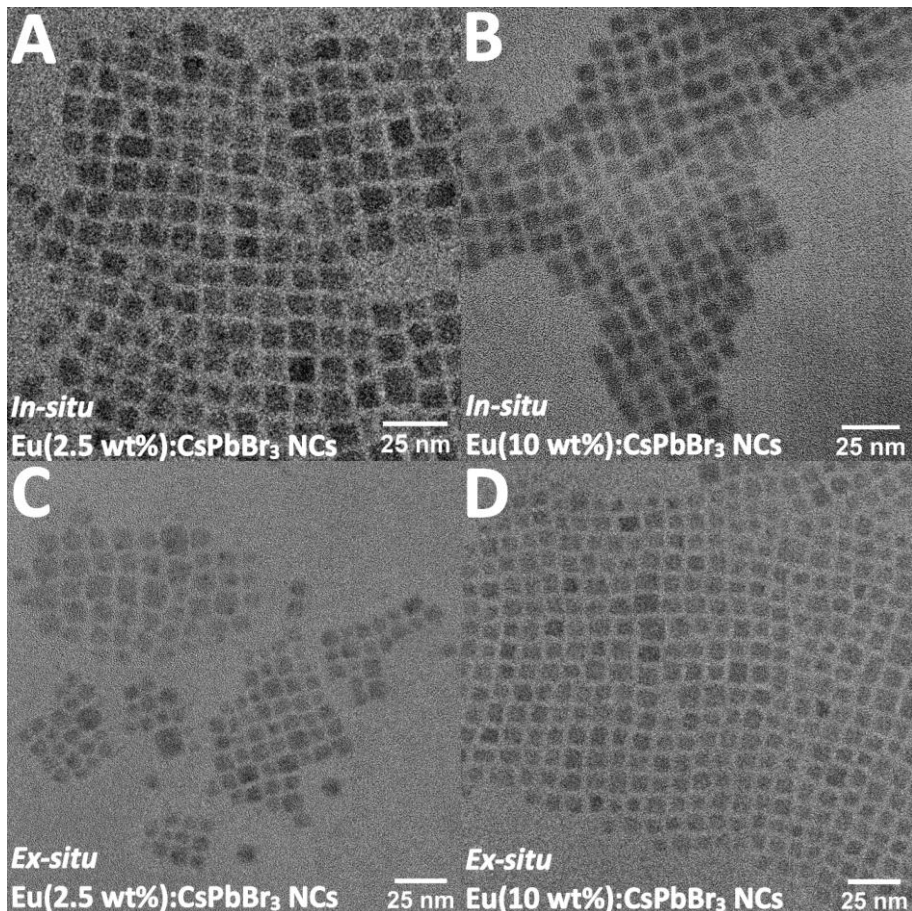
Figure S1: TEM image of in-situ and ex-situ Eu ions doped CsPbBr₃ NCs with different weight percent of Eu: (A, C) 2.5 and (B, D) 10 wt% Eu ions.
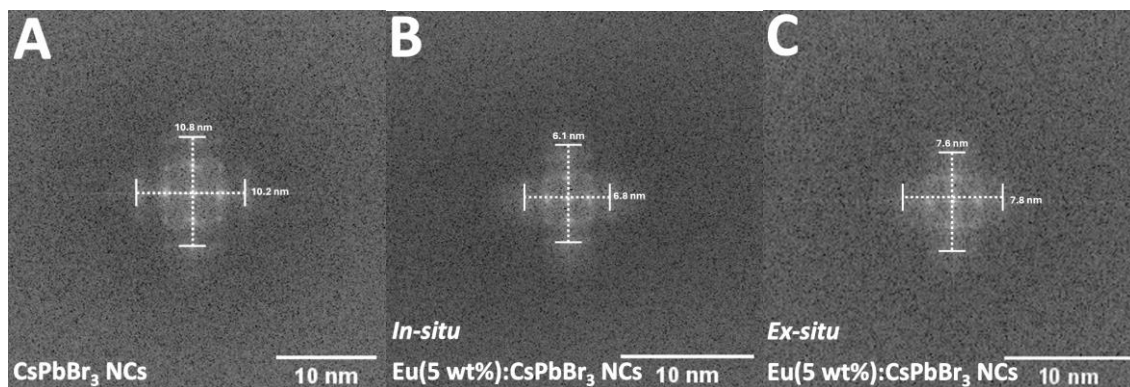
Figure S2: The Fast Fourier Transform (FFT) patterns extracted from TEM images in Figure 1 of (A) CsPbBr$_3$ NCs, (B) in-situ Eu(5 wt%):CsPbBr$_3$ NCs and (C) ex-situ Eu(5 wt%):CsPbBr$_3$ NCs. *Note that Eu(5 wt%):CsPbBr$_3$ NCs refers to the Eu-doped CsPbBr$_3$ NCs, with the value in parentheses indicating the nominal Eu-dopant concentration.*

Table S1: Results of the semi-quantitative EDS analysis for both in-situ and ex-situ Eu ions doped CsPbBr$_3$ NCs. Note that Eu(XX wt%):CsPbBr$_3$ NCs refers to the Eu-doped CsPbBr$_3$ NCs, with the value in parentheses indicating the nominal Eu-dopant concentration.

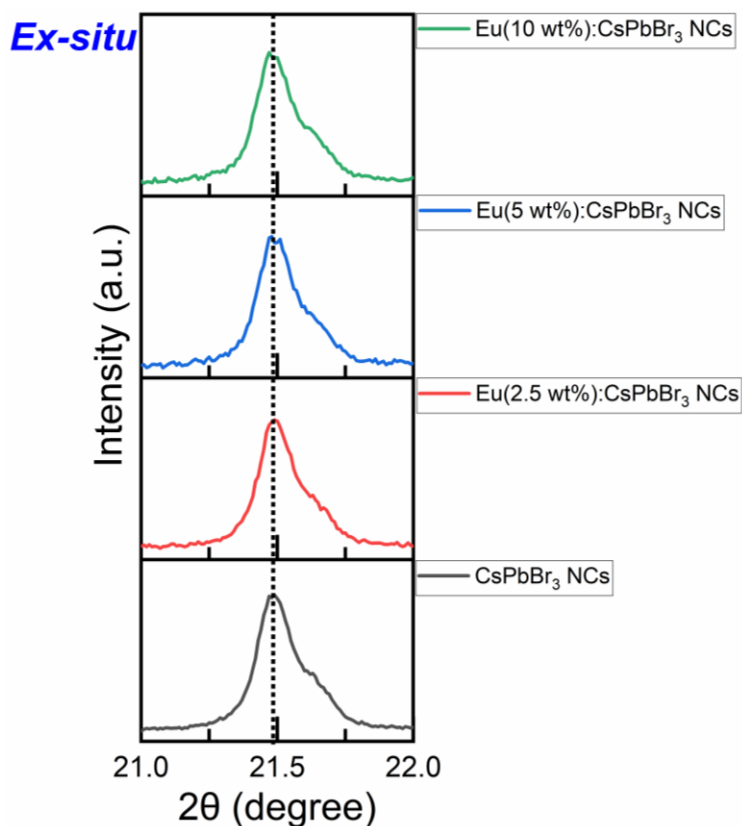|		Cesium (Cs) (at%)	Lead (Pb) (at%)	Bromine (Br) (at%)	Europium (Eu) (at%)
Undoped	CsPbBr$_3$ NCs	19.5%	20.9%	59.6%	-
In-situ doped	Eu (2.5 wt%): CsPbBr$_3$ NCs	19.8%	20.6%	58.9%	0.7%
	Eu (5 wt%): CsPbBr$_3$ NCs	19.2%	19.6%	60.4%	0.8%
	Eu (10 wt%): CsPbBr$_3$ NCs	20.7%	21.1%	57.0%	1.2%
Ex-situ doped	Eu (2.5 wt%): CsPbBr$_3$ NCs	19.8%	20.1%	57.9%	2.2%
	Eu (5 wt%): CsPbBr$_3$ NCs	19.0%	19.2%	57.3%	4.5%
	Eu (10 wt%): CsPbBr$_3$ NCs	17.2%	18.6%	51.8%	12.4%

Figure S3: Enlarged XRD patterns of CsPbBr₃ ex-situ Eu-doped CsPbBr₃ NCs with different Eu³⁺ doping at 21°–22°.

Table S2: XPS spectra for Cs 3d, Pb 4f, Br 3d, and Eu 3d in CsPbBr₃ NCs and for *in-situ* and *ex-situ* Eu-doped (10 wt%) CsPbBr₃ NCs.

	Undoped CsPbBr₃ NCs	*In-situ* doped Eu (10 wt%): CsPbBr₃ NCs	*Ex-situ* doped Eu (10 wt%): CsPbBr₃ NCs
Cs 3d			
Pb 4f			

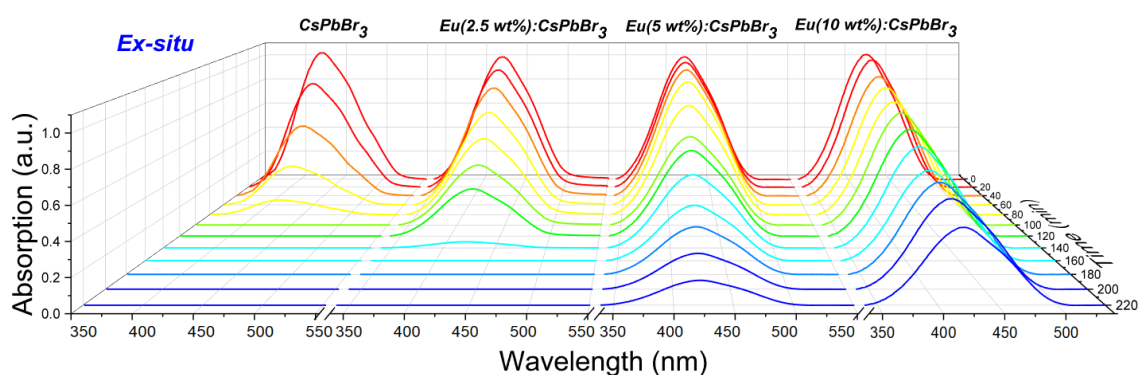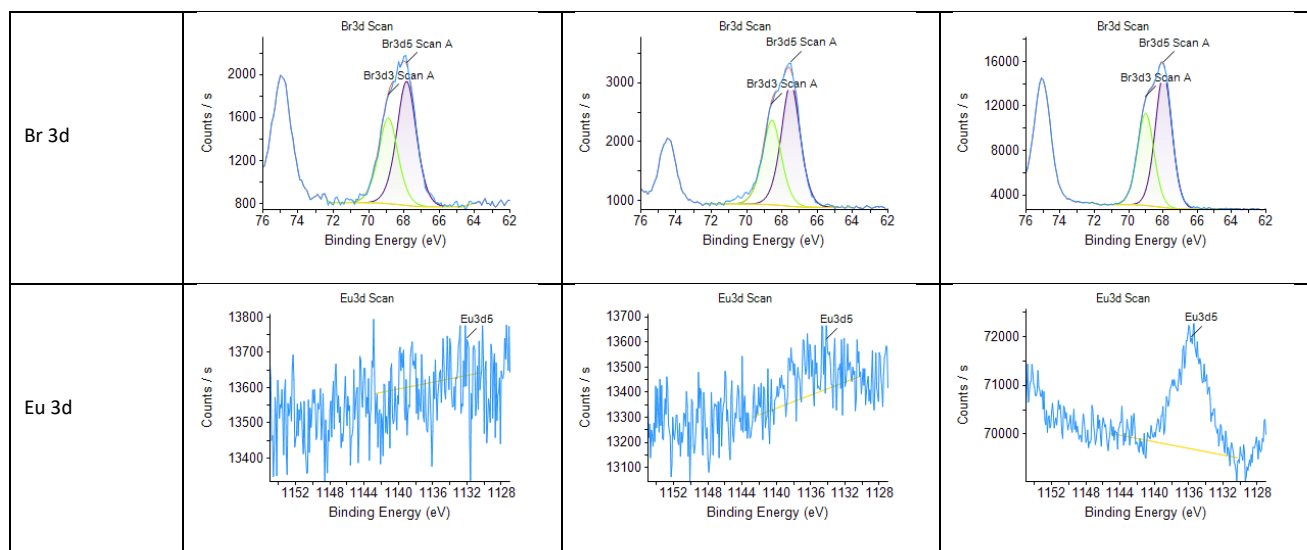|			
Br 3d	Br3d Scan / Br3d5 Scan A / Br3d3 Scan A	Br3d Scan / Br3d5 Scan A / Br3d3 Scan A	Br3d Scan / Br3d5 Scan A / Br3d3 Scan A
Eu 3d	Eu3d Scan / Eu3d5	Eu3d Scan / Eu3d5	Eu3d Scan / Eu3d5

Figure S4: 3D UV-visible spectra of MO photodegradation after different light irradiation times using CsPbBr$_3$ NCs and ex-situ Eu^{3+}-doped CsPbBr$_3$ NCs with varying weight percentages.
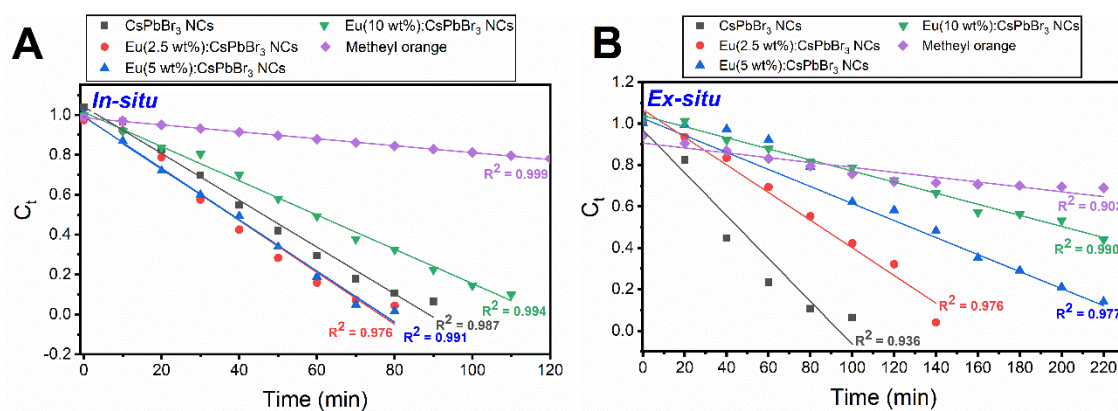
Figure S5: The zero-order kinetic plot of methyl orange (MO) under light illumination for (A) in-situ Eu^{3+}-doped $CsPbBr_3$ NCs and (B) ex-situ Eu^{3+}-doped $CsPbBr_3$ NCs with varying weight percentages.